Non-peer reviewed preprint under review at the Journal of Coastal Research

Title	SCI-OBS: Detection and Classification of People on the Beach and in the Surf Zone
Authors	Michael Reinwald[1], Ketron Mitchell-Wynne[1], Zane D'Amico[1], Mercedes Stringer[1], Benjamin Freeston[1]
Affiliation	[1]Surfline/Wavetrak, Inc., San Francisco, CA, USA
Corresponding author	Michael Reinwald <mreinwald@surfline.com>
ORCID	`https://orcid.org/0000-0001-8481-8392`
License	Creative Commons Attribution–NonCommercial 4.0 International (CC BY-NC 4.0)
Index words	computer vision; deep learning; video monitoring; remote sensing; recreation; water safety; image analysis

A condensed 2-page extended abstract covering an earlier stage of this work was accepted at the 39th International Conference on Coastal Engineering (ICCE 2026), Galveston, TX, 17–22 May 2026, and is forthcoming in the conference proceedings (DOI not yet assigned). The present manuscript is substantially expanded and supersedes it as the complete account of the work.

SCI-OBS: Detection and Classification of People on the Beach and in the Surf Zone

Michael Reinwald*[1], Ketron Mitchell-Wynne[1], Zane D'Amico[1], Mercedes Stringer[1], and Benjamin Freeston[1]

[1]Surfline/Wavetrak, Inc., San Francisco, CA, USA

Abstract

Understanding how many people use beaches and surf zones, and what they are doing there, is vital for safety, tourism and coastal management. Camera-based studies of coastal recreation have to date recovered attendance: a headcount, sometimes divided into coarse zones. This paper reports the accuracy at which the same infrastructure resolves attendance into activity composition, using a multi-class detector deployed in Surfline Coastal Intelligence's coastal monitoring pipeline. The detector is a one-stage convolutional architecture fine-tuned on 27,712 manually-labelled coastal-camera frames, validated on 1,400 frames recorded under clear visibility at 14 sites in Australia, the United Kingdom and the United States against five out-of-the-box baseline models. Each baseline is given its best achievable operating point on the validation data while the presented model is held at its production threshold, so the reported margins are lower bounds. The model attains the highest precision (94.8%), recall (78.5%) and F1-score (85.8%) of the systems evaluated, and its F1 exceeds every baseline's at every confidence threshold; its margin over the strongest baseline is 3.0 F1 points, with a site-level bootstrap interval excluding zero. False detections make up 5.2% of its reported count, less than half the share carried by the two closest baselines, whose aggregate counts rely in part on false positives cancelling missed subjects. Each detected person is then resolved into a recreation type: on-sand and in-water use separate with 97.2% accuracy, and eight activity classes are typed at 83.6% support-weighted and 70.1% macro-averaged accuracy. Resolving a frame's headcount into typed on-sand and in-water counts costs 0.73 subjects per frame over the untyped count of the same subjects. That breakdown is the form coastal-management and water-safety applications require, and no general-purpose person detector can produce it.

Index words: *computer vision, deep learning, video monitoring, remote sensing, recreation, water safety, image analysis.*

1 Introduction

Understanding how people use beaches is essential for a range of coastal stakeholders — from surf businesses and tourism operators to lifeguards and local governments. Accurate usage data helps optimise staffing and safety operations, informs infrastructure planning, and unlocks insights into beachgoer and surfer behaviour. There are also economic factors: recreational surfing has been shown to generate substantial annual value for the communities around individual surf breaks (Lazarow, 2007), underscoring the importance of understanding how coastal spaces are used.

Historically, beach-user data was collected through manual headcounts (Dwight *et al.*, 2007; King and McGregor, 2012; Williams and Lemckert, 2007), which are often inaccurate, limited in coverage, and lack repeatability (Deacon and Kolstad, 2000; Herrera *et al.*, 2024; Koon *et al.*, 2021). Automated video-based systems have since emerged as a promising solution, enabling continuous and high-frequency monitoring (Guillén *et al.*, 2008; Lee *et al.*, 2019). Guillén *et al.* (2008) used Argus systems for hourly counts over four years, revealing daily, seasonal, and inter-annual usage patterns. More recently, Murray *et al.* (2023) used an earlier-generation version of SCI-OBS to estimate in-water surfer counts and ride durations over 2,500 hours of footage at a high-use Australian surf break.

While these studies demonstrate progress, most systems still face key challenges: limited coverage and difficulty detecting in-water users (especially surfers) due to occlusion, glare, wave interference, and the small apparent size of subjects. Aerial surveys using drone (Herrera *et al.*, 2024) or aircraft (Provost *et al.*, 2021) platforms can offer high-resolution snapshots over large areas but are typically conducted on a monthly or seasonal basis, limiting their applicability for continuous monitoring. In contrast, fixed coastal cameras provide a stable, long-term monitoring solution.

This paper presents SCI-OBS, the multi-class object detector of the Surfline Coastal Intelligence (SCI) pipeline, trained on a large commercial network of fixed coastal cameras and designed to operate reliably across both beaches and surf zones under varying environmental conditions. SCI-OBS resolves the people it detects into eight classes: beachgoers standing, sitting, lying or wading, surfers paddling, sitting or surfing, and stand-up paddleboarders. This paper validates detection and recreation-type classification over those classes.

Prior camera-based work on coastal recreation recovers attendance, a headcount sometimes split into coarse zones (the Related Work subsection below). This paper reports the accuracy at which the same infrastructure resolves each person into an activity type across a network of sites, characterising a deployed system against widely-used out-of-the-box baselines on a manually-labelled coastal validation set. Comparison against external census ground truth, such as lifeguard counts or drone surveys, is left to future work.

The remainder of the paper is structured as follows. The Related Work subsection that follows situates this work against prior efforts to quantify coastal recreation from cameras. The Methods section describes the relevant part of the SCI coastal monitoring pipeline and how SCI-OBS fits within it, then the model architecture, training data, validation dataset, and evaluation metrics. The Results section reports people-detection performance against five out-of-the-box baselines. The Discussion section covers the effect of domain-specific training, the composition of the count error, the operational value of the typing, and the scope within which the results hold; the Conclusions section closes.

1.1 Related Work

Prior work on automated coastal-recreation monitoring spans three methodological families: manual-census and survey methods, aerial / drone imagery, and fixed-camera video analysis.

1.1.1 Manual and Survey-Based Counts

The foundational literature on beach attendance has relied on manual counts conducted by lifeguards, survey teams, or infrastructure operators (Dwight *et al.*, 2007; King and McGregor, 2012; Williams and Lemckert, 2007). These studies established the ecological, economic, and safety value of quantifying beach usage, but also documented the practical limitations: manual methods are labour-intensive, sparse in time, inconsistent across sites, and prone to observer bias (Deacon and Kolstad, 2000; Koon *et al.*, 2021).

1.1.2 Aerial and Drone Surveys

Drone and low-altitude aerial imagery can produce high-resolution snapshots of beach usage over large areas (Herrera *et al.*, 2024; Provost *et al.*, 2021). These methods are effective for episodic campaigns but are typically constrained to monthly or seasonal sampling cadence by operational and regulatory constraints, limiting their applicability for continuous monitoring or rapid response.

1.1.3 Fixed Coastal Cameras

Fixed shore-mounted cameras enable continuous, high-frequency monitoring at a single site. Within this family, early deployments used the Argus coastal-video infrastructure (Guillén *et al.*, 2008) to produce hourly counts over multi-year observation windows. More recent work has focused on integrating modern deep-learning detectors with existing commercial camera infrastructure. Lee *et al.* (2019) applied vision-based safety warning systems at Haeundae Beach, Korea. Most directly related to the present work, Murray *et al.* (2023) applied an earlier-generation version of SCI-OBS to Surfline's commercial camera network at a high-use Australian surf break. Earlier reports from the present authors (Reinwald *et al.*, 2026a, 2026b) also used previous-generation detectors under different validation conventions, so their figures characterise different systems rather than earlier points on the same curve.

The limitations common to this literature are well documented: difficulty detecting small, partially-occluded, or backlit subjects; sensitivity to the specific environmental and geometric conditions of each camera; and the high cost of scaling a single-site pipeline to a globally-distributed network. SCI-OBS is designed to address the third limitation by training once against the diversity of the SCI pipeline's full camera network rather than tuning per-site. Against the first, the detection of small and partially-occluded subjects, it relies on coastal-domain training data rather than on any architecture-side adaptation.

A distinct literature addresses dense-crowd counting directly, either by regressing a density map (Li, Zhang, and Chen, 2018) or by point supervision (Song *et al.*, 2021), and reports strong per-frame counts on crowded scenes. Those methods are not benchmarked here because their output type differs: they return a count or a set of points rather than a classified bounding box. The SCI pipeline consumes individual boxes, for cross-frame tracking and count de-duplication, for geo-referencing against per-camera transects, and for recreation typing. The comparison here is therefore against detectors, the class of system that could substitute for SCI-OBS in the pipeline without a large-scale coastal ground-truth dataset.

Across all three families the quantity recovered is attendance: how many people are present, sometimes separated into a small number of coarse zones. Guillén *et al.* (2008) report beach-user counts over four years without distinguishing bathers from sunbathers, and Herrera *et al.* (2024) count people from drone imagery. The in-water surfer counts of Murray *et al.* (2023) are the closest prior work to a typed count, for one class at one break. Management questions that depend on activity, such as how many of those present are exposed to the water, are not answerable from a headcount. This paper extends the measurable quantity from attendance to activity composition across a network of sites, and quantifies the accuracy at which that is currently possible.

2 Methods

This section describes the pipeline the detector runs inside and the camera network it draws on, then the model and its training corpus, the baseline systems and how they were run, the class taxonomy and the scope of the evaluation, the validation dataset, the metrics, and the confidence-threshold protocol that sets each model's operating point.

2.1 System Architecture

SCI-OBS operates as one inference stage within a production video-analytics pipeline. The camera network it draws on and the processing chain it sits in both bound what the detector is given and what is done with its output.

2.1.1 Camera Network and Study Sites

Surfline Coastal Intelligence operates a global network of commercial pan-tilt-zoom (PTZ) surf cameras at coastal locations worldwide. The cameras are commercial IP surveillance units from a mix of vendors, mounted on elevated structures, with zoom and field of view configurable remotely.

To evaluate SCI-OBS's detection performance under varied conditions, a representative subset of 14 camera sites was selected spanning Australia, the United Kingdom, and the United States (Table 1). The selected cameras span a range of user densities, environmental conditions, and perspectives, varying in placement, view, and lighting across the network. Figure 1 shows the geographic distribution of the full camera network and the regions the study sites are drawn from; Figure 2 shows example frames from six of the selected sites with ground-truth bounding boxes overlaid.

2.1.2 Processing Pipeline

Each recorded video segment is processed through the SCI pipeline, a GPU-accelerated inference stack built on NVIDIA DeepStream (NVIDIA, 2019). Individual video segments ("rewinds") of approximately 10 minutes' duration are processed through a modular stack of neural-network and analytical models, including the SCI-OBS detector described here.

Table 1: The 14 commercial coastal-camera sites making up the validation benchmark, with the country each is located in. The sites span three countries and both hemispheres, and cover a range of user densities, camera geometries and lighting conditions. The table allows the geographic and environmental spread of the benchmark to be assessed directly. Five 20-frame clips were drawn from each site, giving the 1,400 frames used throughout.

Camera	**Country**
Currumbin Alley	AU
Kirra	AU
Snapper Rocks	AU
Bantham	UK
Fistral	UK
Rest Bay	UK
New Smyrna	US
Steamer Lane	US
Tourmaline	US
Lower Trestles	US
Huntington Beach	US
Huntington Beach Overview	US
Middles (Saltcreek)	US
17th Street	US

SCI-OBS runs on every rewind, independently of atmospheric conditions. In production, rewinds flagged as degraded by an upstream visibility classifier (Reinwald *et al.*, 2026c) — fog, rain, lens spray or strong glare — are excluded from the aggregated counts, so those aggregates are robust to conditions under which per-rewind detections would be unreliable.

2.2 Model and Training Data

SCI-OBS is an Ultralytics YOLO26-L end-to-end object detector (Ultralytics, 2025), a modern one-stage detector, fine-tuned on Surfline's coastal-camera dataset. The architecture is used in its publisher-supplied reference configuration, with no coastal-specific modifications.

SCI-OBS was trained on a proprietary coastal-camera dataset of 27,712 manually-labelled frames carrying 600,303 labels across eight person classes (Table 2). The frames come from 457 distinct camera sites across the network, spanning a wide range of environmental and visual conditions. Annotations were created and quality-controlled by a team of trained analysts working to a consistent labelling protocol.

The detector was fine-tuned from the publisher-supplied COCO checkpoint. Standard augmentation was applied throughout, including dynamic brightness, contrast, hue and saturation adjustment to improve invariance under variable lighting. Model selection used a seeded, camera-stratified 90/10 split of the pool, the 10% holdout of which also supplies the calibration split

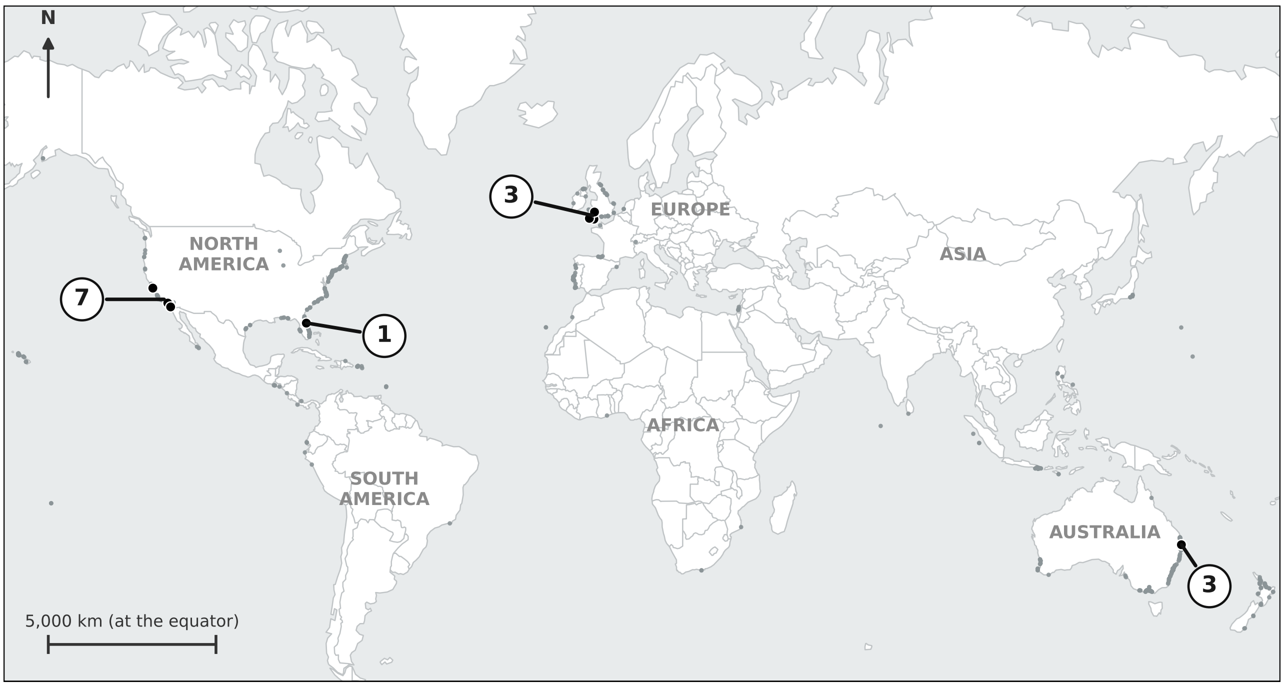

Figure 1: Geographic distribution of the coastal-camera network. Grey dots mark every commercially deployed camera carrying coordinates; larger black dots mark the 14 validation cameras. Ringed white discs annotate the four regions those cameras are drawn from, labelled with the number from each: seven from the western United States, one from the eastern United States, three from the United Kingdom and three from Australia. Sites are listed in Table 1. The figure establishes that the evaluation draws on a globally distributed fleet rather than a single site or region. Mercator projection, north-up, with a north arrow at the upper left and a scale bar at the lower left; the bar is true along the equator, since scale on a Mercator projection varies with latitude. Continents are labelled for orientation. Camera positions are as of August 2026.

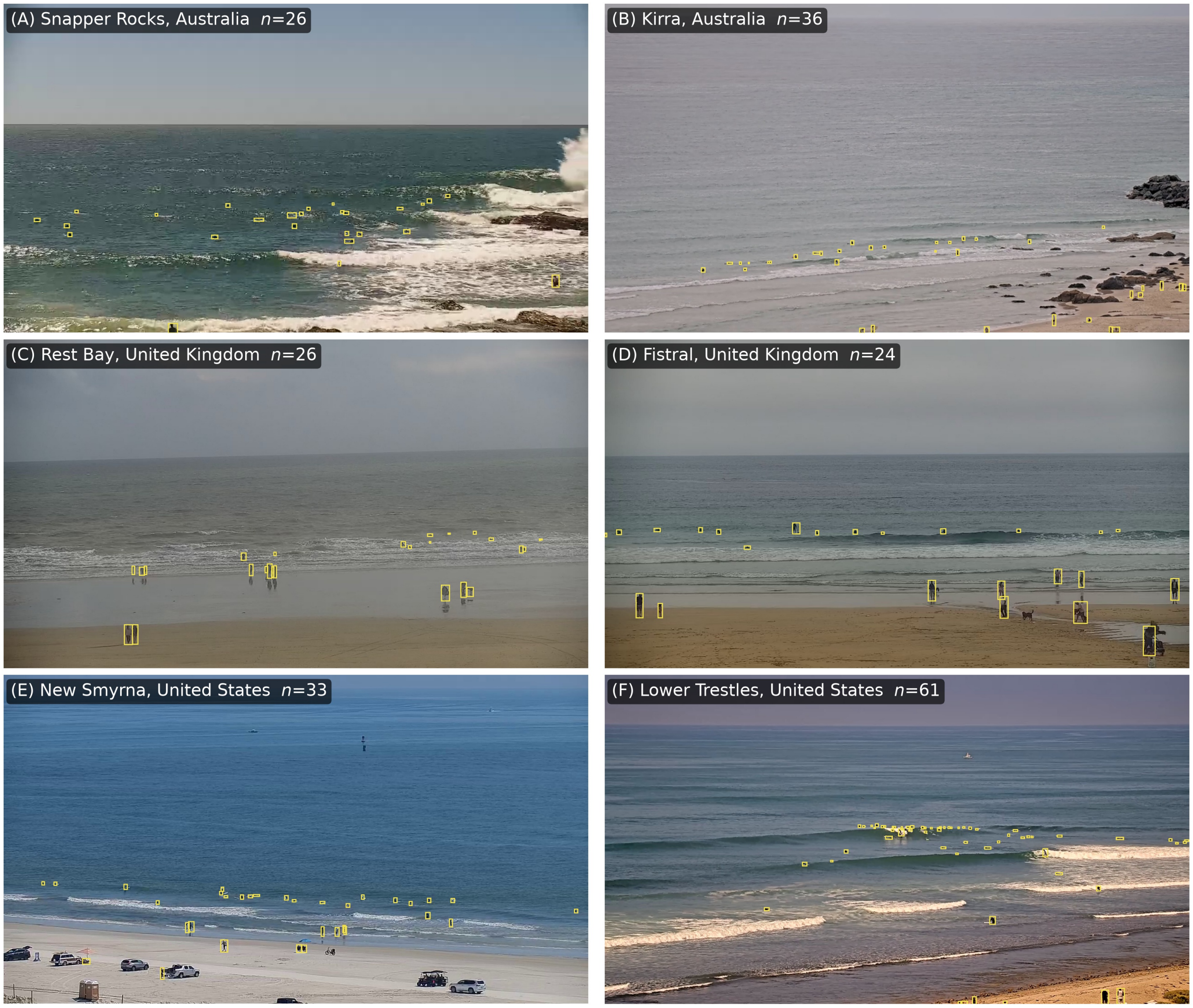

Figure 2: Example frames from six of the 14 validation sites, two from each country represented: (A) Snapper Rocks and (B) Kirra, Australia; (C) Rest Bay and (D) Fistral, United Kingdom; (E) New Smyrna and (F) Lower Trestles, United States. Yellow rectangles are the manually-assigned ground-truth person labels. The panels differ in camera elevation and zoom, in the fraction of the frame occupied by water, and in the apparent pixel size of individual subjects. The panels indicate the range of viewing geometry, subject density and lighting that one detector has to handle across the network. The full site list is given in Table 1.

of the Confidence-Threshold Protocol subsection.

Table 2: Class distribution of the training corpus: labelled bounding-box instances per class over its 27,712 frames, ordered by count. The corpus is the training pool only; the 14-site validation benchmark is not part of it. The distribution shows the class imbalance under which the classifier is trained, which is why the recreation-type results are reported both support-weighted and macro-averaged.

Class	**Labelled instances**
Surfer (sitting)	224,880
Beachgoer (standing)	128,057
Surfer (paddling)	111,085
Beachgoer (sitting)	61,430
Beachgoer (wading)	39,096
Surfer (surfing)	20,896
Beachgoer (lying)	12,358
Stand-up paddleboard	2,501

2.3 Benchmark Models and Inference Configuration

SCI-OBS was benchmarked against five out-of-the-box detectors evaluated on the same validation dataset using their publishers' reference weights with no coastal fine-tuning:

1. YOLO26-L (COCO-only) (Ultralytics, 2025) — the same architecture as SCI-OBS, loaded from publisher-supplied COCO-pretrained weights rather than coastally fine-tuned. Referred to as YOLO26-L (and YOLO26-L + SAHI for the SAHI-enhanced variant).

2. RT-DETR-L (COCO-only) (Zhao *et al.*, 2024) — a state-of-the-art transformer-based detector from its publisher-supplied COCO-pretrained weights. Referred to as RT-DETR-L (and RT-DETR-L + SAHI).

3. MMDetection with SAHI (Akyon, Altinuc, and Temizel, 2022), referred to as MMDET-SAHI.

YOLO26-L is the same detector architecture as SCI-OBS, trained on the COCO general-purpose dataset rather than on Surfline's coastal data. Any performance gap between SCI-OBS and YOLO26-L is therefore attributable to training data alone, not to architectural differences. The RT-DETR-L pair extends the comparison to a different modern architecture family (transformer-based) to confirm that the pattern is not architecture-specific. SAHI (Slicing Aided Hyper Inference) (Akyon, Altinuc, and Temizel, 2022) variants apply image tiling (512×512 slices with 0.2 overlap) at inference time, which is the standard technique for improving small-object detection without re-training. MMDET-SAHI spans a third architecture family: a two-stage region-proposal detector, structurally unlike both the one-stage YOLO and the transformer. SCI-OBS and the YOLO26-L and RT-DETR-L baselines (with and without SAHI) were run with Ultralytics 8.4.38 and SAHI 0.11.36. MMDET-SAHI was run with MMDetection 3.3.0, MMCV 2.1.0, and SAHI 0.11.35 (Cascade Mask R-CNN R50-FPN 1× COCO reference weights).

YOLO26-L has no peer-reviewed architectural description: it is defined by its implementation, cited here as a software release rather than as a publication. Both SCI-OBS and the COCO-pretrained baselines are pinned to Ultralytics 8.4.38 and the reference weights that release distributes, so the comparison holds the implementation fixed and varies the training corpus.

All systems were fed frames at an input width of 1,408 pixels. SCI-OBS is served as an FP16 TensorRT engine with a 768 × 1,408 input, which preserves the source aspect ratio and matches the rectangular-batch training described above. The YOLO26-L baselines, run through Ultralytics, also preserve aspect ratio, letterboxing a 16:9 frame to an effective 1,408 × 800; RT-DETR-L instead rescales each frame to a square 1,408 × 1,408, which is the mapping that architecture is designed around. Remaining inference parameters were left at the Ultralytics 8.4.38 defaults.

2.4 Class Taxonomy and Evaluation Scope

SCI-OBS is a multi-class detector, trained on eight fine-grained person classes: beachgoers in different postures (standing, sitting, lying, wading), surfers in different states (paddling, sitting, surfing), and stand-up paddleboarders.

For the comparison against the general-purpose baselines the eight classes are collapsed into a single "People" category: those baselines' training corpora know only one "person" class, so a like-for-like comparison has to aggregate SCI-OBS's outputs to that level. The fine-grained typing, which runs in production across the network, is evaluated separately in the Recreation-Type Classification subsection. Figure 3 shows a representative SCI-OBS detection for each class.

2.5 Validation Dataset

For this study, inference was applied to a controlled validation dataset consisting of 70 short video sequences: five 20-frame clips sampled at 1 Hz from each of the 14 selected camera sites described in the Camera Network and Study Sites subsection. These clips were drawn from different times and scenes, yielding a total of 1,400 frames containing 64,130 ground-truth labels. Ground truth was produced in a single annotation pass by the team described above, working to one proto-

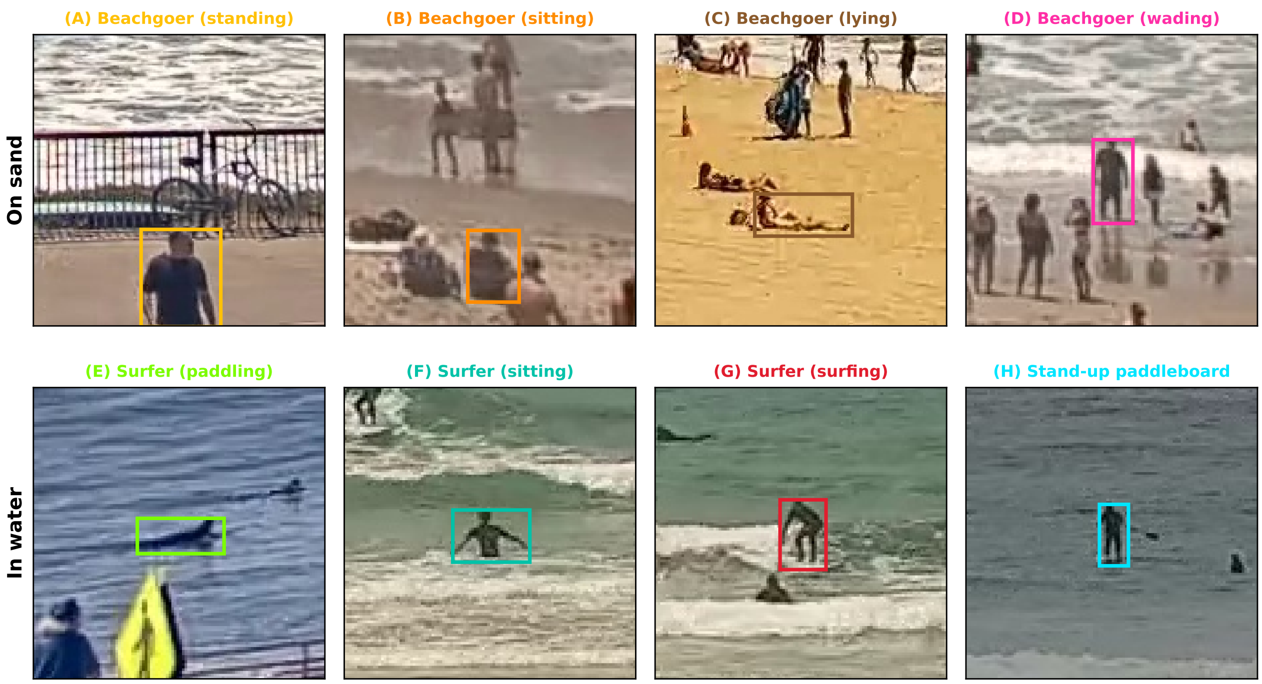

Figure 3: Representative SCI-OBS detections for the eight person classes in the fine-grained taxonomy, in two rows: (A) beachgoer standing, (B) beachgoer sitting, (C) beachgoer lying and (D) beachgoer wading on the on-sand row, and (E) surfer paddling, (F) surfer sitting, (G) surfer surfing and (H) stand-up paddleboarder on the in-water row. Each crop shows a single predicted detection; box colour and label give the predicted class. The gallery shows what each recreation class looks like at coastal-camera range, which is the distinction the classifier is required to make. Crops are illustrative; per-class accuracy is given in Table 6.

col; no subsample was double-annotated, so no inter-annotator agreement estimate is available. The benchmark is held out at the frame and clip level: none of the 1,400 frames appears in the training corpus, none of the 70 clips does, and no benchmark camera contributes a training frame from any calendar day the benchmark is drawn from. All 14 cameras do, however, contribute training frames from other days: 1,775 of the 27,712 images in the training pool, of which 1,511 come from the Huntington Beach pier camera alone and the remaining thirteen contribute between 1 and 70 images each.

2.6 Evaluation Metrics

Three standard detection metrics assess performance: precision, recall, and F1-score. Detection outcomes are computed per frame and aggregated for overall performance. Precision (Equation 1) quantifies the proportion of true positives (TP) relative to predictions, recall (Equation 2) reflects the model's ability to recover ground-truth objects, and the F1-score (Equation 3) is the harmonic mean of precision and recall:

$$P = \frac{\mathrm{TP}}{\mathrm{TP} + \mathrm{FP}} \tag{1}$$

$$R = \frac{\mathrm{TP}}{\mathrm{TP} + \mathrm{FN}} \tag{2}$$

$$F_1 = \frac{2 \cdot P \cdot R}{P + R} \tag{3}$$

A prediction counts as a true positive when its intersection-over-union with a ground-truth box exceeds a threshold, and matching is one-to-one, so a prediction can claim at most one ground-truth box and vice versa. Metrics are reported at an IoU threshold of 0.1. The downstream consumer of these detections is a per-frame counting and aggregation pipeline, which requires each detection to be uniquely associable with a subject but does not use its precise extent; at the apparent subject sizes in these frames, a few pixels across, stricter thresholds measure localisation accuracy that the counting task does not depend on.

Two count statistics summarise the same detections at the frame level. The mean absolute error (MAE) is the mean over frames of the absolute difference between the predicted and ground-truth counts. The count-recovery rate is the total number of detected individuals divided by the total number of ground-truth individuals across all frames; because it aggregates before differencing, within-frame false positives can offset missed detections, so it is read alongside the miss and false-positive rates rather than on its own. Predicted counts are also regressed on ground-truth counts by ordinary least squares, which separates a systematic departure from the identity line, given by the fitted slope, from the unsystematic part, given by the residual standard deviation.

2.7 Confidence-Threshold Protocol

Every detector emits a confidence score per predicted box, and every reported metric depends on the threshold above which boxes are kept. Each model is therefore reported at an explicitly calibrated operating point.

SCI-OBS is reported at a threshold of 0.25, which is calibrated without reference to the validation dataset: it derives from the 10% of the training pool held out for model selection during training. No quantity derived from the validation dataset informs SCI-OBS's operating point. Each baseline, by contrast, is deliberately given its F1-optimal threshold on the validation dataset itself, found by sweeping in steps of 0.01 and selecting the F1 maximum — by construction the best operating point the model can achieve on the reported data. Any calibration bias in this asymmetric protocol favours the baselines, so the reported margins are lower bounds.

Two of the five baseline optima coincide with the model's own inference floor rather than falling inside the swept range: for YOLO26-L + SAHI and MMDET-SAHI the floor is a hyperparameter of the slicing merge rather than a threshold that can be swept below, so their reported figures are the best available at the reference floor.

3 Results

Detection accuracy bounds everything derived from it, so it is reported first, followed by the frame-level counts those detections produce and the recreation typing applied to them. All figures are computed on the 14-site benchmark, with each system at the operating point fixed in the Confidence-Threshold Protocol subsection.

3.1 Detection Performance

SCI-OBS attains the highest precision, recall and F1-score of the six systems evaluated at the IoU 0.1 operating point: 94.8%, 78.5% and 85.8% (Table 3). Every baseline figure in that table is the model's best achievable operating point on this dataset while SCI-OBS is held at its production threshold, so the reported margins are lower bounds. The two tiled baselines come closest, YOLO26-L + SAHI at 82.8 F1 and RT-DETR-L + SAHI at 78.6; the untiled systems trade recall away, recovering little more than half the subjects present.

The architecture-matched pair is the informative comparison. YOLO26-L differs from SCI-OBS only in training data and sits 11.1 F1 points lower. Tiling recovers most of that gap, and does so unevenly: it closes 83% of the missed-detection gap for YOLO26-L and 84% for RT-DETR-L, bringing the tiled baselines within 4.8% and 15.6% of SCI-OBS's miss count, but only 69% and 41% of their false-positive gaps, leaving them at 2.2 and 3.7 times its false-positive count.

A cluster bootstrap over the 14 sites, 20,000 draws, places the margin over YOLO26-L + SAHI at a 95% interval of $[+1.0, +5.1]$ F1 points and the margin over YOLO26-L at $[+9.2, +13.2]$; all five margins exclude zero. Table 5 gives each model's inference floor, its F1-optimal threshold on this benchmark and the smallest margin SCI-OBS holds over it across the sweep.

Per-site results are given in Table 4. F1 varies by 16 points across the benchmark and orders approximately with scene density, the four densest sites each carrying over six thousand ground-truth labels and accounting for a disproportionate share of the aggregate error. SCI-OBS records the highest F1 at 13 of the 14 sites. The exception is Kirra, where YOLO26-L + SAHI reaches 94.0 against SCI-OBS's 87.9 at almost identical precision, recovering more of the subjects present. Training overlap does not order the table, and with 14 sites and overlap confounded with density no inference is drawn from that.

Table 3: Per-frame detection outcomes — true positives, false positives and false negatives, with the precision, recall and F1-score derived from them (in percent) — for SCI-OBS and the five out-of-the-box benchmark models on the 1,400-frame validation dataset (14 sites, 64,130 ground-truth labels) at IoU threshold 0.1. Each baseline is evaluated at its F1-optimal confidence threshold on this dataset; SCI-OBS is held at its production threshold of 0.25, calibrated on held-out training data (the Confidence-Threshold Protocol subsection). The raw counts are given so that every derived quantity quoted in the text can be recomputed; this table is the reference for every detection figure in the paper. Rows are ordered by F1, best first, and the best precision, recall and F1 are set in bold.

Model	TP	FP	FN	P	R	F1
SCI-OBS	50319	2786	13811	**94.8**	**78.5**	**85.8**
YOLO26-L+SAHI	49656	6133	14474	89.0	77.4	82.8
RT-DETR-L+SAHI	48170	10274	15960	82.4	75.1	78.6
YOLO26-L	46363	13560	17767	77.4	72.3	74.7
MMDET-SAHI	35778	6121	28352	85.4	55.8	67.5
RT-DETR-L	36883	15449	27247	70.5	57.5	63.3

3.2 Count Recovery and Error Composition

SCI-OBS posts a count MAE of 8.15 individuals per frame and recovers 82.8% of the ground-truth count (Figure 4). The tiled baselines edge that aggregate error, but the composition of their counts differs: false positives make up 5.2% of SCI-OBS's reported count, against 11.0% and 17.6% for the two tiled baselines and 22.6% for the untiled YOLO26-L, whose near-complete recovery consists in part of false detections offsetting the subjects it misses. Table 3 carries the per-model figures.

Table 4: Per-site detection performance at IoU threshold 0.1, ordered by scene density (ground-truth labels per site, densest first). **GT** is the number of ground-truth person labels at that site across its five 20-frame clips and **Train** the number of training-pool images contributed by that camera. The three F1 columns are **F1** for SCI-OBS and **Y+S** and **R+S** for the two strongest baselines, YOLO26-L + SAHI and RT-DETR-L + SAHI, each at the operating point used throughout; the pooled row reproduces Table 3. F1 in percent, the first two columns in counts. The table shows the per-site variation that the pooled figures conceal, and how it relates to scene density and training overlap. Huntington Pier and Huntington Pier (ov.) are the close-up and overview cameras at the same location.

Site	GT	Train	F1	Y+S	R+S
Middles	7,810	9	82.2	81.7	76.6
Huntington Pier (ov.)	7,104	18	86.2	85.1	81.2
Huntington Pier	6,413	1,511	81.8	73.8	68.6
Lower Trestles	6,230	70	90.8	87.5	76.7
17th Street	5,857	14	77.7	76.7	72.8
Currumbin Alley	5,131	9	79.2	71.4	75.8
Tourmaline	4,976	21	91.8	88.3	83.3
New Smyrna	4,252	20	88.3	86.4	79.9
Kirra	3,790	1	87.9	94.0	91.1
Rest Bay	2,677	26	89.0	86.2	83.7
Fistral	2,660	24	93.8	93.1	90.5
Steamer Lane	2,509	20	87.7	83.3	77.1
Snapper Rocks	2,477	15	87.7	73.0	76.1
Bantham	2,244	17	88.6	83.7	80.7
Pooled	64,130	1,775	**85.8**	82.8	78.6

Table 5: Confidence-threshold sweeps behind the reported operating points, from sweeps in steps of 0.01. **Floor** is the model's inference floor, below which its predictions cannot be generated; **Opt.** the F1-optimal threshold on this benchmark; **F1*** the F1 there; and **F1†** the F1 at SCI-OBS's production threshold of 0.25, calibrated on held-out training data and quoted throughout the paper. **Min.** is the smallest F1 advantage SCI-OBS holds over that baseline at any threshold where both are defined, with the threshold at which it occurs. ‡optimum coincides with the inference floor. F1 in percent. The table shows where each operating point sits relative to the model's swept range, and that SCI-OBS leads at every threshold at which a baseline is defined.

Model	Floor	Opt.	F1*	F1†	Min.
SCI-OBS	0.01	0.16	87.0	85.8	—
YOLO26-L + SAHI	0.10	0.10‡	82.8	—	+3.6@0.10
RT-DETR-L + SAHI	0.10	0.18	78.6	—	+8.3@0.19
YOLO26-L	0.01	0.06	74.8	—	+9.2@0.04
MMDET-SAHI	0.05	0.05‡	67.5	—	+16.5@0.05
RT-DETR-L	0.01	0.17	63.3	—	+23.7@0.17

Regressing predicted on ground-truth counts separates the systematic and unsystematic parts of that error. SCI-OBS has the shallowest slope of the four models plotted, 0.771 against 0.694 to 0.873 for the baselines, so it undercounts the densest frames the most in proportional terms. It also has much the least scatter about its own fit, a residual standard deviation of 4.8 subjects per frame against 7.3, 9.3 and 11.1.

Decomposed into misses and false positives, SCI-OBS averages 9.9 and 2.0 per frame against a mean of 45.8 ground-truth people, the fewest of both among the models evaluated; YOLO26-L + SAHI is closest at 10.3 and 4.4.

Figure 5 shows the highest-density frame at each of three sites with ground-truth boxes alongside the predictions of SCI-OBS and the two tiled baselines, each at its reported operating point. Per-panel n is the number of boxes drawn and so includes false positives.

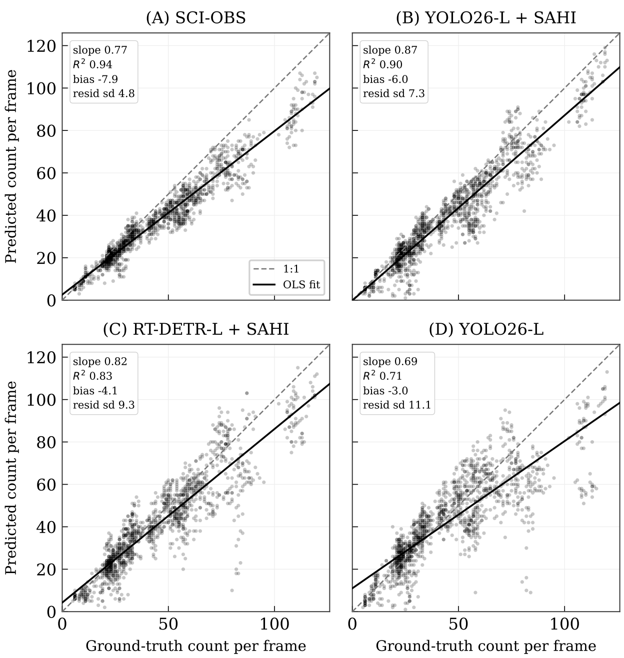

Figure 4: Per-frame predicted counts against ground-truth counts for the four models with the highest F1, as a two-by-two grid of scatter panels sharing one identity line and one pair of axes: (A) SCI-OBS, (B) YOLO26-L + SAHI, (C) RT-DETR-L + SAHI and (D) YOLO26-L. Each of the 1,400 validation frames contributes one point; the markers are partly transparent, so darker regions are frames whose counts coincide. The dashed line is 1:1 and the solid black line an ordinary least-squares fit, annotated with its slope, R^2, mean signed error and residual standard deviation. The panels separate the two ways a per-frame count can be wrong: a systematic slope departure from 1:1, and scatter about the fitted line. The two models not shown (MMDET-SAHI and RT-DETR-L) lie further from the identity line; their numerical results are in Table 3.

3.3 Recreation-Type Classification

Every ground-truth box in the validation set carries a manually-assigned recreation state (the Validation Dataset subsection), so this typing is evaluated on the same 14-site benchmark. The metric is classification given detection: of the people SCI-OBS detects, matched to a ground-truth box at IoU 0.1 by spatial overlap alone, the fraction whose predicted class equals the ground-truth class. This isolates typing quality from detection recall.

On-sand versus in-water use is recovered with 97.2% accuracy: a detected beachgoer is almost never mistaken for a water user (Figure 6). That figure is conditioned on detection and weighted by class support, and the residual cross-block confusion concentrates at the sitting-surfer/wading waterline interface, where upright people stand at the water's edge.

At the finer eight-class level the picture depends on how classes are weighted, and both weightings are reported (Table 6). Support-weighted accuracy is 83.6%; the macro-average over the eight classes is 70.1% recall and 83.3% precision. Sitting surfers account for 47.8% of the labels scored, so the support-weighted figure is dominated by that class.

Typed counts compose detection and typing. Against ground-truth means of 30.4 in-water and 15.2 on-sand subjects per frame, SCI-OBS returns 24.9 and 13.1, a mean absolute error of 5.83 and 2.97 respectively. The untyped count over the same subjects has an error of 8.07 per frame, so typing adds 0.73 subjects per frame.

4 Discussion

Three readings of the reported figures bear on how the detector should be used rather than on how it scores. They concern where coastal training contributes over inference-time remedies, which of the two count statistics matters for a monitoring product, and what the recreation typing is worth in operation. The scope within which all three hold closes the section.

4.1 Effect of Domain-Specific Training

Slicing-aided inference is the standard remedy for small objects, and it is the intervention a practitioner would reach for before acquiring labels. On this benchmark it recovers most of what the architecture-matched baseline lacks in recall but little of what it lacks in precision (the Detection Performance subsection): after tiling, both baselines sit within a sixth of SCI-OBS's missed-detection count while still returning two to four times as many false positives. A larger pixel budget lets a general-purpose detector find small subjects; it does not tell it which candidates in a breaking-wave field are

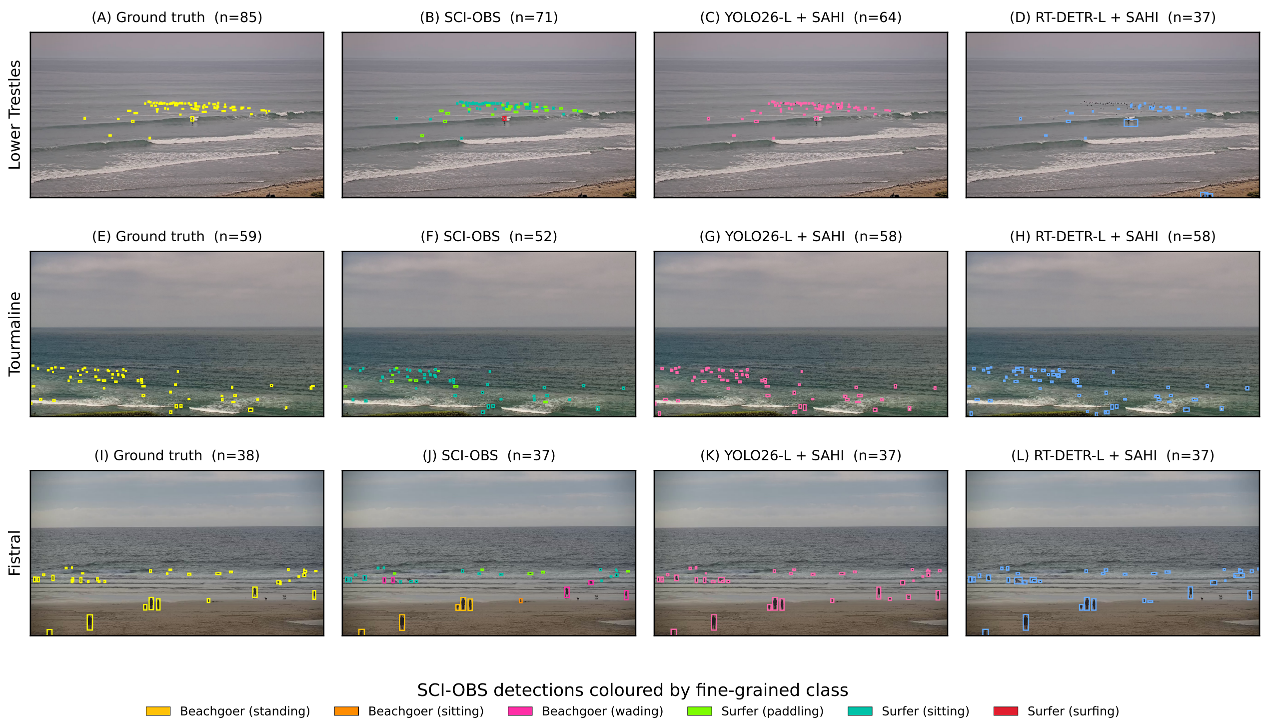

Figure 5: Bounding-box overlays on the highest-density ground-truth frame at each of three sites, as twelve panels labelled (A) to (L) left to right and top to bottom. The rows are Lower Trestles (A–D), Tourmaline (E–H) and Fistral (I–L); the columns are ground truth (yellow), SCI-OBS (coloured by fine-grained class, legend below), YOLO26-L + SAHI (pink) and RT-DETR-L + SAHI (blue). Per-panel n is the number of boxes drawn and therefore includes false positives. The rows show how the aggregate metrics arise on the densest frames at each site, where most of the validation labels lie.

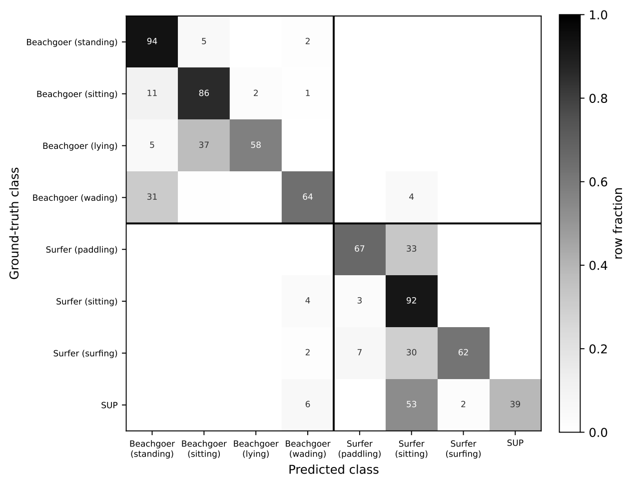

Figure 6: Recreation-type classification of SCI-OBS over the people it detects, as a row-normalised confusion matrix (percentage of each ground-truth class; rows sum to 100), with ground-truth class on the rows, predicted class on the columns and cell shading proportional to percentage. Black rules separate the on-sand classes (top-left block) from the in-water classes (bottom-right block). Cross-block confusion corresponds to 97.2% on-sand/in-water accuracy, conditioned on detection and weighted by class support. The matrix shows where the typing errors fall, and in particular that they concentrate between visually similar classes within a block rather than across the sand/water boundary. Because the matrix is row-normalised it shows recall only; per-class precision and ground-truth support are given in Table 6.

Table 6: Recreation-type classification given detection, per class, over the 50,169 subjects SCI-OBS detects out of the 63,790 validation labels carrying one of the eight recreation states. **GT** is the number of ground-truth instances of that class in the benchmark; recall is the fraction of detected instances of the class typed correctly (the diagonal of Figure 6) and precision the fraction of instances predicted as that class whose ground-truth class matches (its column). Both are restricted to detected subjects. Reading precision alongside recall identifies which classes are reliable in both directions and which are under-predicted. The macro average weights the eight classes equally, the support-weighted accuracy by prevalence.

Recreation type	**GT**	**R**	**P**	**F1**
Beachgoer (standing)	8,461	0.935	0.717	0.812
Beachgoer (sitting)	4,311	0.859	0.835	0.847
Beachgoer (lying)	1,042	0.575	0.700	0.632
Beachgoer (wading)	7,464	0.641	0.777	0.702
Surfer (paddling)	10,759	0.666	0.863	0.752
Surfer (sitting)	30,496	0.925	0.875	0.899
Surfer (surfing)	1,112	0.617	0.953	0.749
Stand-up paddleboard	145	0.389	0.947	0.551
Macro average	—	0.701	0.833	—
Support-weighted	63,790	0.836 accuracy		

people. The same decomposition appears in a convolutional and a transformer detector, which locates it in the training distribution rather than in either architecture, and it is the reverse of the direction in which both tiling and domain fine-tuning are usually argued for.

4.2 Systematic and Residual Count Error

The two count statistics rank the systems differently, and the disagreement is informative. On aggregate error the tiled baselines edge SCI-OBS; on scatter about their own fitted line they are worse by a factor of one and a half to two. For a monitoring product the second matters more. A proportional undercount is a single scale factor, estimable once per camera from a modest number of labelled frames and applied thereafter; residual scatter cannot be calibrated away and propagates into every derived quantity, including the peak-occupancy and trend statistics a coastal manager reads. SCI-OBS trades a steeper systematic undercount for materially less of the error that cannot be corrected.

4.3 Operational Value of the Recreation Typing

Detection accuracy bounds what the typing can achieve, but it is the typing that determines what the output is useful for. A headcount answers how many people are present; the eight-class breakdown answers how many are exposed to the water, which is the quantity coastal-safety and management applications act on. The general-purpose baselines cannot produce it at any inference cost, since their taxonomy has one class where this one has eight. The cost of producing it is modest: resolving a frame's headcount into typed on-sand and in-water counts adds 0.73 subjects per frame to the error of the untyped count (the Recreation-Type Classification subsection). Figure 7 shows the typing across representative sites and conditions.

4.4 Scope and Limitations

The figures reported above hold within four conditions: they are computed on single frames, sampled under clear visibility, from cameras that also contribute to the training corpus, and scored against a reference annotation whose own error rate is unmeasured. None of the four can be lifted by further analysis of the present benchmark.

Single-Frame Evaluation. Cross-frame temporal consistency, tracking and count de-duplication are handled by downstream post-processing modules of the SCI pipeline and are not evaluated here.

Visibility. The benchmark samples clear-visibility sessions, so the conditions varied are subject density, distance and viewing geometry rather than atmospheric visibility. Per-rewind performance under heavy fog, rain, lens spray or strong glare is not characterised. In production SCI-OBS runs on those rewinds, but downstream aggregation excludes any flagged as degraded.

Benchmark Camera Composition. SCI-OBS is not deployed on unseen cameras: labels are acquired for a camera, the detector is retrained, and the retrained model is deployed on that camera, so a camera in service is one the model has seen, and the benchmark matches that condition. All 14 benchmark cameras contribute frames to the training corpus, though never the same clips or days, and the overlap is uneven (the Validation Dataset subsection). The reported figures accordingly do not establish performance on a camera absent from training, which would require a leave-camera-out study.

Reference Standard and Sparse Classes. The reported precision has an unquantified ceiling: the reference annotation was produced in a single pass without a double-annotated subsample, so no inter-annotator agreement estimate is available (the Validation Dataset subsection). The likelier of the two error modes at 45.8 subjects per frame is a missed annotation, which is scored against the detector as a false positive, so the reported precision is more plausibly conservative than flattering. Two classes are also too thinly sampled to characterise, stand-up paddleboarders and lying beachgoers, and the non-person classes are not evaluated because the benchmark carries no labels for them.

5 Conclusions

This paper has characterised the people-detection and recreation-type classification performance of SCI-OBS, the multi-class object detector of the Surfline Coastal Intelligence pipeline, against five out-of-the-box detectors on a 1,400-frame, 14-site validation dataset. SCI-OBS attains the highest precision (94.8%), recall (78.5%) and F1-score (85.8%) of all systems evaluated, with every baseline given its F1-optimal threshold on the validation data while SCI-OBS runs at its production threshold calibrated on held-out training data. A site-level bootstrap places the margin over the strongest baseline at 3.0 F1 points (95% interval 1.0 to 5.1) and over the same architecture without coastal training at 11.1 points (9.2 to 13.2).

The advantage over the matched architecture is unevenly distributed across error types. Slicing-aided inference, the standard method for increasing per-object pixel budget, closes 83% of the missed-detection gap for YOLO26-L and 84% for RT-DETR-L, but only 69% and 41% of their false-positive gaps. Both tiled baselines end within 5% and 16% of SCI-OBS on missed detections while returning 2.2 and 3.7 times as many false positives. Coastal training therefore contributes predominantly to precision at these subject sizes, and inference-time tiling to recall.

SCI-OBS resolves each detected person into a recreation type, separating on-sand from in-water use at 97.2% accuracy and typing eight activity classes at 83.6% support-weighted and 70.1% macro-averaged accuracy. Typed counts cost 0.73 subjects per frame beyond the untyped count of the same subjects. Camera-based studies of coastal recreation have to date recovered attendance; these results establish the accuracy at which the same infrastructure resolves attendance into activity composition. The accuracy is sufficient for the on-sand and in-water split to be used directly, and lower at the waterline: wading beachgoers, the class most relevant to water safety, are recovered at 0.641 recall, so wading counts should be treated as lower bounds.

The architecture is an off-the-shelf YOLO26-L in its reference configuration, and no architectural contribution is claimed. Three limits bound the results. The benchmark samples clear-visibility sessions, so performance under fog, rain, lens spray and strong glare is uncharacterised. All benchmark cameras contribute training frames, consistent with the labels-then-retrain operating model but leaving performance on an unlabelled camera an open question that a leave-camera-out study

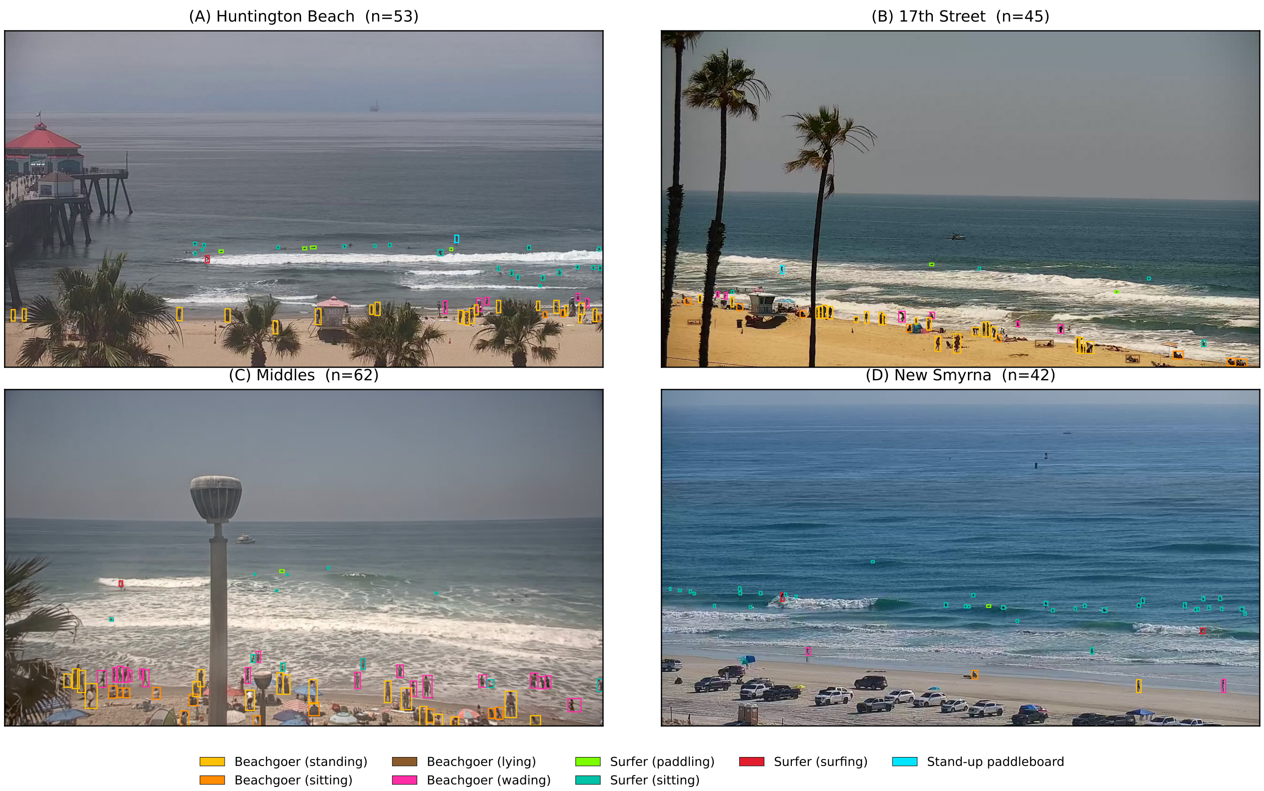

Figure 7: SCI-OBS fine-grained class predictions at four sites, as a two-by-two grid of full frames: (A) Huntington Beach, (B) 17th Street, (C) Middles and (D) New Smyrna. Every SCI-OBS person detection is drawn and coloured by its predicted class (see legend), with warm tones for the on-sand beachgoer classes and cool tones for the in-water surfer and stand-up-paddleboarder classes. The panels show the typing operating across differing views, lighting and subject densities. Per-panel n is the SCI-OBS person count. Examples are illustrative; per-class accuracy is given in Table 6.

would address. Two classes, stand-up paddleboarders at 145 benchmark instances and lying beachgoers at a fifth detected, are too thinly sampled to characterise. Comparison against vision–language models prompted for coastal-scene counting would establish whether the reported advantage persists against systems trained at web scale.

Acknowledgements

An earlier version of this work was posted as a non-peer-reviewed preprint on EarthArXiv (Reinwald *et al.*, 2026a), and a condensed two-page extended abstract covering an earlier stage of the work is forthcoming in the proceedings of the 39th International Conference on Coastal Engineering (Reinwald *et al.*, 2026b). Both are precursors to the present version.

B. Freeston, a co-author of this paper, is the named inventor on US Patent 10,891,481 B2 (Freeston, 2021), assigned to Surfline/Wavetrak, Inc., which discloses the broader automated ocean-sensing framework within which SCI-OBS was developed.

All authors are employees of Surfline/Wavetrak, Inc., which develops and commercially operates the SCI pipeline and the SCI-OBS detector evaluated in this paper, and which funded the work. No external funding was received.

The training dataset, the validation annotations and the fine-tuned model weights are proprietary and are not released. The base architecture (Ultralytics YOLO26-L, release 8.4.38, in its reference configuration), the confidence-threshold protocol and the validation-dataset composition (14 camera sites, 70 clips, 1,400 frames, 64,130 labels) are documented in this paper. No comparable coastal-camera detection benchmark is publicly available, so the figures reported here cannot at present be reproduced on equivalent data.

Literature Cited

Akyon, F.C.; Altinuc, S.O., and Temizel, A., 2022. Slicing aided hyper inference and fine-tuning for small object detection. *Proceedings of the 2022 IEEE International Conference on Image Processing (ICIP)* (Bordeaux, France), pp. 966–970.

Deacon, R.T. and Kolstad, C.D., 2000. Valuing beach recreation lost in environmental accidents. *Journal of Water Resources Planning and Management*, 126(6), 374–381.

Dwight, R.H.; Brinks, M.V.; SharavanaKumar, G., and Semenza, J.C., 2007. Beach attendance and bathing rates for Southern California beaches. *Ocean & Coastal Management*, 50(10), 847–858.

Freeston, B., 2021. *Automated Detection of Features and/or Parameters within an Ocean Environment Using Image Data*. Alexandria, Virginia: United States Patent and Trademark Office, U.S. Patent No. 10,891,481 B2, assigned to Surfline/Wavetrak, Inc.

Guillén, J.; García-Olivares, A.; Ojeda, E.; Osorio, A.; Chic, Ó., and González, R., 2008. Long-term quantification of beach users using video monitoring. *Journal of Coastal Research*, 24(6), 1612–1619.

Herrera, C.; Connolly, R.M.; Rasmussen, J.A.; McNamara, G.; Murray, T.P.; Lopez-Marcano, S.; Moore, M.; Campbell, M.D., and Alvarez, F., 2024. Drone insights: Unveiling beach usage through AI-powered people counting. *Drones*, 8(10), 579.

King, P. and McGregor, A., 2012. Who's counting: An analysis of beach attendance estimates and methodologies in southern California. *Ocean & Coastal Management*, 58, 17–25.

Koon, W.; Schmidt, A.; Queiroga, A.C.; Sempsrott, J.; Szpilman, D.; Webber, J., and Brander, R., 2021. Need for consistent beach lifeguard data collection: Results from an international survey. *Injury Prevention*, 27(4), 308–315.

Lazarow, N., 2007. The value of coastal recreational resources: A case study approach to examine the value of recreational surfing to specific locales. *In:* Lemckert, C. (ed.), *Proceedings of the 9th International Coastal Symposium* (Gold Coast, Queensland, Australia). *Journal of Coastal Research*, Special Issue No. 50, pp. 12–20.

Lee, J.; Park, J.; Kim, I., and Kang, D.Y., 2019. Application of vision-based safety warning system to Haeundae Beach, Korea. *In:* Lee, J.L.; Yoon, J.-S.; Cho, W.C.; Muin, M., and Lee, J. (eds.), *The 3rd International Water Safety Symposium. Journal of Coastal Research*, Special Issue No. 91, pp. 216–220.

Li, Y.; Zhang, X., and Chen, D., 2018. CSRNet: Dilated convolutional neural networks for understanding the highly congested scenes. *Proceedings of the 2018 IEEE/CVF Conference on Computer Vision and Pattern Recognition (CVPR)* (Salt Lake City, Utah), pp. 1091–1100.

Murray, T.; Greaves, M.; Da Silva, G.; Boyle, O.; Wynne, K.; Freeston, B.; Ditria, L.; Jardine, P.; Ditria, E.; Strauss, D.; Tomlinson, R., and Burton, P., 2023. Utilising object detection from coastal surf cameras to assess surfer usage. *Proceedings of the Australasian Coasts & Ports Conference 2023* (Sunshine Coast, Queensland, Australia). doi:10.3316/informit.472912089750558

NVIDIA, 2019. *DeepStream SDK: Accelerating Real-Time AI-Based Video and Image Analytics*. `https://developer.nvidia.com/deepstream-sdk`.

Provost, E.J.; Coleman, M.A.; Butcher, P.A.; Colefax, A.; Schlacher, T.A.; Bishop, M.J.; Connolly, R.M.; Gilby, B.L.; Henderson, C.J.; Jones, A.; Lastra, M.; Maslo, B.; Olds, A.D., and Kelaher, B.P., 2021. Quantifying human use of sandy shores with aerial remote sensing technology: The sky is not the limit. *Ocean & Coastal Management*, 211, 105750.

Reinwald, M.; Mitchell-Wynne, K.; D'Amico, Z.; Stringer, M., and Freeston, B., 2026a. SCI-OBS: Detection and classification of people on the beach and in the surf zone. *EarthArXiv*, non-peer-reviewed preprint. doi:10.31223/X5VV3X

Reinwald, M.; Stringer, M.; Wynne, K.; D'Amico, Z., and Freeston, B., 2026b. SCI-OBS: Reliable object detection for monitoring coastal recreation. *Proceedings of the 39th International Conference on Coastal Engineering* (Galveston, Texas), in press.

Reinwald, M.; Mitchell-Wynne, K.; D'Amico, Z.; Stringer, M., and Freeston, B., 2026c. SCI-VIS: Lightweight visibility tagging for coastal camera monitoring. *EarthArXiv*, non-peer-reviewed preprint. doi:10.31223/X5FN5W

Song, Q.; Wang, C.; Jiang, Z.; Wang, Y.; Tai, Y.; Wang, C.; Li, J.; Huang, F., and Wu, Y., 2021. Rethinking counting and localization in crowds: A purely point-based framework. *Proceedings of the 2021 IEEE/CVF International Conference on Computer Vision (ICCV)* (Montreal, Canada), pp. 3365–3374.

Ultralytics, 2025. *Ultralytics YOLO.* `https://github.com/ultralytics/ultralytics`.

Williams, P. and Lemckert, C., 2007. Beach carrying capacity: Has it been exceeded on the Gold Coast? *In:* Lemckert, C. (ed.), *Proceedings of the 9th International Coastal Symposium* (Gold Coast, Queensland, Australia). *Journal of Coastal Research*, Special Issue No. 50, pp. 21–24.

Zhao, Y.; Lv, W.; Xu, S.; Wei, J.; Wang, G.; Dang, Q.; Liu, Y., and Chen, J., 2024. DETRs beat YOLOs on real-time object detection. *Proceedings of the 2024 IEEE/CVF Conference on Computer Vision and Pattern Recognition (CVPR)* (Seattle, Washington), pp. 16965–16974.